nature materials

LETTERS

https://doi.org/10.1038/s41563-021-01001-7

Check for updates

Large-scale growth of few-layer two-dimensional black phosphorus

Zehan Wu[1,2], Yongxin Lyu[1,2], Yi Zhang[1], Ran Ding[1], Beining Zheng[1], Zhibin Yang[1], Shu Ping Lau[1], Xian Hui Chen[3]✉ and Jianhua Hao[1,2]✉

Two-dimensional materials provide opportunities for developing semiconductor applications at atomistic thickness to break the limits of silicon technology. Black phosphorus (BP), as a layered semiconductor with controllable bandgap and high carrier mobility, is one of the most promising candidates for transistor devices at atomistic thickness[1–4]. However, the lack of large-scale growth greatly hinders its development in devices. Here, we report the growth of ultrathin BP on the centimetre scale through pulsed laser deposition. The unique plasma-activated region induced by laser ablation provides highly desirable conditions for BP cluster formation and transportation[5,6], facilitating growth. Furthermore, we fabricated large-scale field-effect transistor arrays on BP films, yielding appealing hole mobility of up to 213 and 617 $cm^2 V^{-1} s^{-1}$ at 295 and 250 K, respectively. Our results pave the way for further developing BP-based wafer-scale devices with potential applications in the information industry.

Black phosphorus (BP), a rediscovered elemental two-dimensional (2D) semiconductor, possesses both appealing carrier mobility and a widely tunable bandgap (E_g) ranging from 0.3 eV in the bulk to around 2 eV for the monolayer[7–9], covering the magnitudes of E_g values of conventional semiconductors used for transistor devices (for example, $E_{g,Si} \sim 1.12$ eV and $E_{g,GaAs} \sim 1.44$ eV). Moreover, BP exhibits a variety of unique properties that are valuable for diverse applications ranging from nanoelectronics and nanophotonics to quantum devices and superconductors[7–12]. Combined, all these features make BP an ideal candidate for 2D applications, enabling it to finally break through development obstacles and lay the foundation for 2D materials in the information industry. Contrary to its promising application prospects, the controllable large-scale growth of few-layer BP films has been a long-standing major problem since the discovery of BP, and the lack of a solution has greatly hindered its further investigation and practical applications. To date, top-down exfoliated BP suffers from limited scale and irregular shape, and furthermore, the red-phosphorus-based allotropic transformation approach does not lead to high-quality films with atomistic thickness[13–15]. Recently, chemical vapour deposition (CVD) enabled the bottom-up synthesis of BP, but only few-layer flakes up to dozens of micrometres in lateral scale have been obtained[16,17]. This might be due to the unique sp^3 hybridization of phosphorus atoms in BP, which results in a higher surface energy than that of the substrate, hindering the lateral layer growth of BP[6]. Furthermore, the construction of the BP phase requires extreme high-pressure conditions, which can barely be achieved in vapour-phase deposition approaches[9]. Here, we report a controlled pulsed laser deposition (PLD) strategy to synthesize high-quality, few-layer BP on the centimetre scale. In combination with molecular dynamics (MD) simulations, we show that, instead of conventional heat-assisted evaporation, the employ of a pulsed laser can facilitate the formation of large BP clusters within the transported physical vapour, thus reducing the formation energy of the BP phase and enabling the large-scale growth of few-layer BP[5,6]. In addition to demonstrating the crystalline homogeneity of the obtained BP over a large area, we made advances by fabricating BP-film-based centimetre-scale field-effect transistor (FET) arrays that exhibit appealing electrical performances that are not only comparable to those of previously reported micrometre-scale BP, but also highly uniform over the entire film, crucially setting the stage for BP-based semiconductor integrated circuits in the information industry.

We achieved centimetre-scale BP growth in an ultrahigh vacuum chamber by using bulk monocrystal BP as the source and mica wafer with a freshly exfoliated surface as the substrate (Fig. 1a; see Methods and Supplementary Fig. 1 for more details). A different reflective colour compared with the bare mica can be observed for the as-grown BP films (Fig. 1b), with the uniform sheen extending over the 1-cm^2 surface of the mica wafer, signifying great potential for the subsequent fabrication of large-scale device arrays. Additionally, precise control of film thickness (that is, layer number) can be readily achieved by manipulating the number of laser pulses during deposition, and a growth rate of ~1.3 Å s^{-1} was deduced (Supplementary Fig. 2). Taking advantage of the ultrahigh homogeneity of the atomic plane of the mica surface and the uniform distribution of BP clusters in the laser-generated physical vapour, unidirectional growth and the merging of monolayer BP flakes are thermodynamically preferred, facilitating the formation of a continuous BP film (Fig. 1c–e and Supplementary Fig. 3). The elemental composition and atom coordination in the obtained BP films were determined by energy-dispersive X-ray spectroscopy (EDX) mapping through high-angle annular dark-field (HAADF) transmission electron microscopy (TEM) and X-ray photoelectron spectroscopy (XPS) measurements. The results show that elemental phosphorus is uniformly distributed across the probed region (Fig. 1f,g). The weak signal from the P–O bond in the P 2*p* XPS spectrum (Fig. 1h) arises from a small amount of surface oxidation during the measurement[18]. Hence, the elemental purity of the as-prepared BP film is evidenced and potential contamination from oxidation can be ruled out.

To identify the large-area continuity and homogeneity of the obtained BP films, a combination of X-ray diffraction (XRD),

[1]Department of Applied Physics, The Hong Kong Polytechnic University, Hong Kong, People's Republic of China. [2]The Hong Kong Polytechnic University Shenzhen Research Institute, Shenzhen, People's Republic of China. [3]Hefei National Laboratory for Physical Sciences at Microscale and Department of Physics, and CAS Key Laboratory of Strongly-coupled Quantum Matter Physics, University of Science and Technology of China, Hefei, People's Republic of China. ✉e-mail: chenxh@ustc.edu.cn; jh.hao@polyu.edu.hk

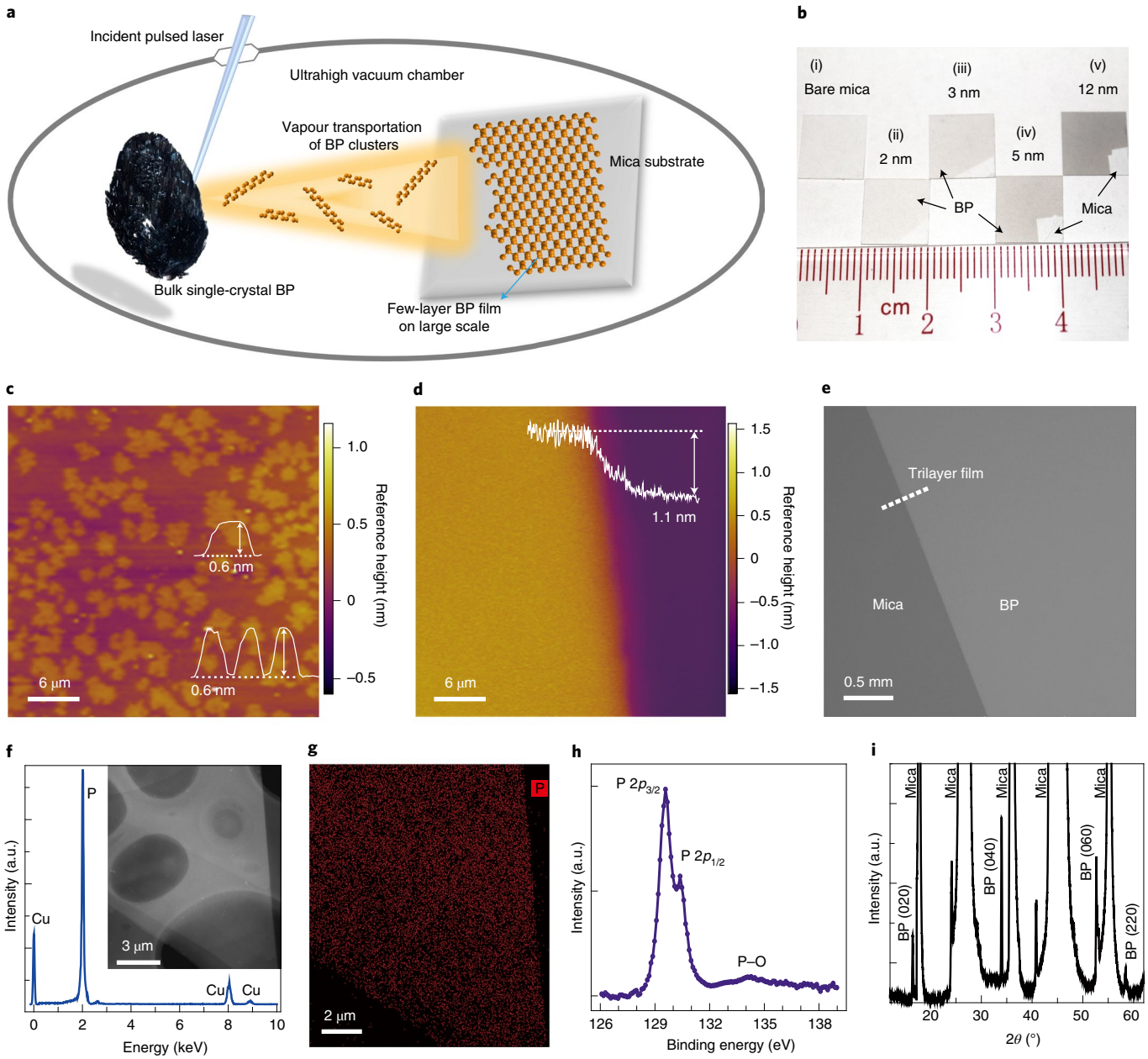

Fig. 1 | Growth of centimetre-scale few-layer BP films. a, Schematic of the controlled PLD process used for the fabrication of few-layer BP films. **b**, Photographs of bare mica (i) and as-deposited centimetre-scale BP films of different thickness (ii–v). **c**, Atom force microscopy (AFM) image showing the topography of monolayer BP flakes synthesized with a few laser pulses. The monolayer thickness is indicated by the inserted height profile. **d**, AFM image showing the thickness of a bilayer BP film. **e**, EBSD image of a trilayer BP film on mica substrate showing the uniformity and continuity surpassing the millimetre scale. **f**,**g**, EDX spectrum (**f**) and elemental mapping (**g**) of an approximate ten-layer BP sample recorded with HAADF-TEM. High elemental purity can be recognized. The inset in **f** shows the TEM image of the scan region. **h**, The P 2*p* XPS spectrum of an approximate ten-layer BP film. A high proportion of chemical bonding states related to typical P–P bonds can be observed. **i**, XRD pattern of the as-synthesized BP. Peaks corresponding to the typical orthorhombic structure of BP are dominant.

electron back-scatter diffraction (EBSD) and polarized Raman mapping measurements were performed. Three main diffraction peaks from (02*n*0) in addition to those of the mica substrate can be observed from the XRD pattern in Fig. 1i. This fingerprint corresponds to the typical orthorhombic structure of the BP crystal[19], providing direct evidence of the large-scale high crystallinity of the as-prepared BP films. Benefiting from the flat surface morphology of our sample, EBSD mapping was performed on the millimetre scale to identify the crystallinity, orientation and uniformity[20,21]. The EBSD orientation mapping images presented in Fig. 2a–c exhibit no distinct boundaries or azimuthal rotations of BP domains, confirming the highly orientated crystal growth of orthorhombic BP along the (010) direction. Further EBSD mapping studies were performed on BP samples with four different layer numbers (Supplementary Fig. 4).

The large-area polarized Raman mapping images shown in Fig. 2d–f provide further insight into the grain distribution of a few-layer BP film. We focused on the characteristic lattice vibration of BP, in particular the A^2_g mode with anisotropic features, to study extended defects such as dislocations and grain boundaries[15,22,23].

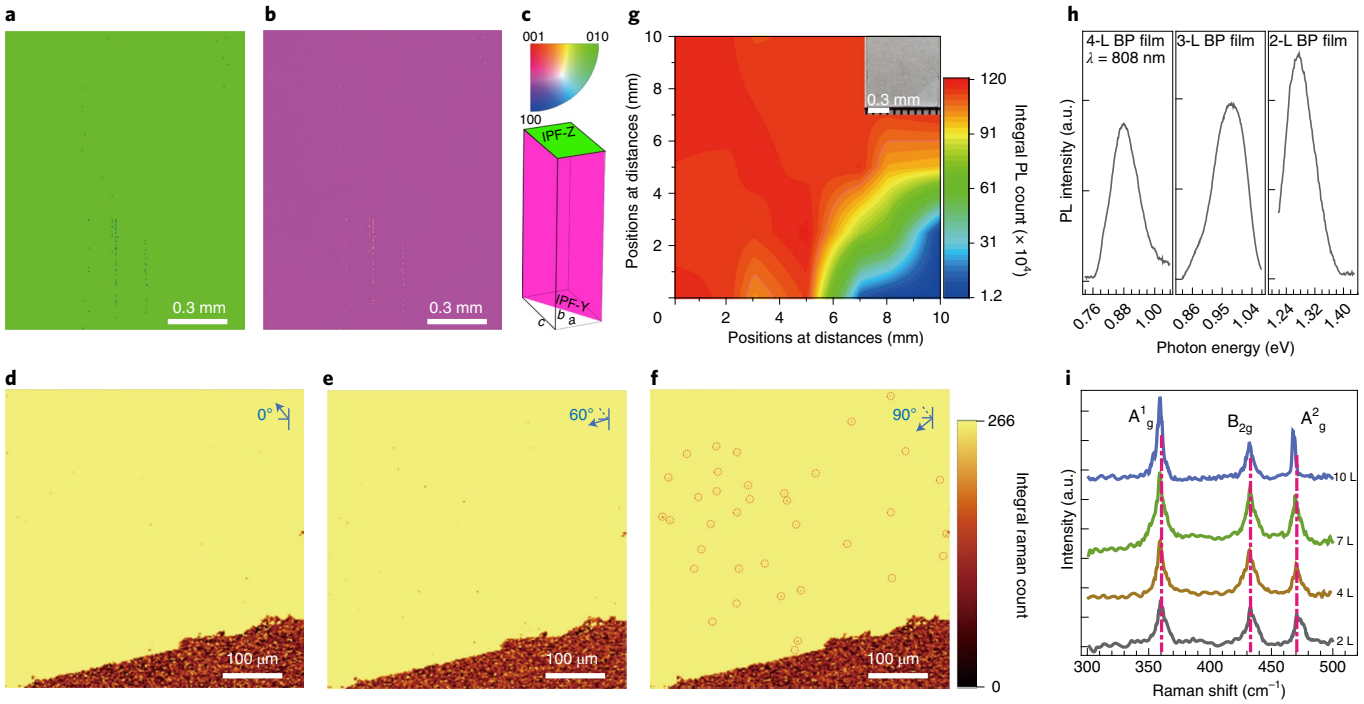

Fig. 2 | Large-area investigations of few-layer BP films. a,b, Inverse pole figures along the *z* axis (IPF-Z, **a**) and *y* axis (IPF-Y, **b**) of an approximate eight-layer BP film, obtained from large-scale EBSD mapping. **c**, Differential colour matching of the IPFs in **a** and **b** with the dominant diffractive crystal plane. **d**–**f**, Large-scale 0° (**d**), 60° (**e**) and 90° (**f**) polarized Raman mapping images of the integrated intensity of the A^2_g peak of an approximate ten-layer BP. The area with low Raman counts in the lower right-hand corner of each image represents the mica substrate. The dotted circles in **f** show the distribution of inhomogeneous signals in the boundaries caused by domain misalignment. **g**, Average PL mapping study comprising 36 scattered-point integrated sampling performed on the top of a three-layer BP film. The inset shows a photograph of the corresponding measured sample with the associated scale. The boundary between the deposited BP film and the bare mica substrate can be seen in the bottom right-hand corner. **h**, Layer-dependent PL characteristics of few-layer BP films. 4-L, four-layer; 3-L, three-layer; 2-L, two-layer. **i**, Raman spectra of few-layer BP films. A slight left-shift of the signals is observed with increasing layer (L) number[8,24].

In particular, we used a polarized 532-nm laser with three characteristic orientations of the polarization state, 0°, 60° and 90°. Given the high sensitivity of 90°-polarized Raman scattering to BP crystal orientation, the observation of dispersive marks without visible grain boundaries evidences the highly homogeneous crystallographic orientation of the BP grains. Further Raman examinations suggested that the angle-dependent anisotropic feature is highly uniform over the 1-cm-size sample. Furthermore, this crystallographic orientation homogeneity was also observed at ultrathin thickness (Supplementary Fig. 5). As further evidence, the photoluminescence (PL) mapping image presented in Fig. 2g exhibits identical E_g across the entire BP film on the centimetre scale. We note that the layered-dependent behaviour observed in the PL and Raman measurements (Fig. 2h,i) is fully consistent with previous studies[8,24]. By combining large-area diffraction techniques and optical spectroscopy measurements, our observations reveal a highly uniform crystal orientation across the as-obtained BP sample on the centimetre scale.

To investigate the microscopic crystal structure of the as-grown BP films, high-resolution TEM (HRTEM) studies were performed. The plan-view image of the approximate eight-layer BP film shown in Fig. 3a displays a highly ordered arrangement of BP atoms without visible defects on the as-grown film. A closer examination of the atomic arrangement pattern in Fig. 3b reveals lattice constants of 3.30 and 4.55 Å along the zigzag and armchair directions, which matches well with the orthorhombic structure of the BP crystal[19]. The ball-and-stick schematic diagrams in Fig. 3b illustrate the AB stacking structure of adjacent BP layers[25]. The corresponding selected-area electron diffraction (SAED) pattern presented in Fig. 3c exhibits a typical orthogonal lattice with homologous quadruple symmetry, highly indicative of the crystalline nature of the as-prepared sample. Furthermore, we used dark-field (DF) TEM diffraction-filtered measurements with a large micrometre aperture filter to investigate the orientation of the BP lattice on the mica substrate. Figure 3d displays the diffraction patterns of randomly selected sections from the same BP sample: we determined an identical lattice orientation in the BP film (red rectangular shape) and the mica substrate (orange hexagonal shape), based on a comparison with the fingerprints of bare mica and BP (Fig. 3e). This feature was found to be highly homogeneous over a large-area BP film (Fig. 3f). Thus, the observation of highly oriented growth of the BP lattice further proves the large-area structural continuity of our BP film.

The longitudinal interlaminar structure of the obtained BP films with various layer numbers was studied by cross-sectional HRTEM (Fig. 3g,h), which revealed well-defined layer structures. We calculated the spacing between neighbouring BP layers to be around 0.53 nm, which is consistent with the well-accepted values of ~0.52–0.56 nm (ref. [26]). Specifically, the unique double-atom-layer characteristic of the BP monolayer can be observed, and distinct stratification of the mica substrate and each BP layer can be recognized through the van der Waals (vdW) vacuum layers. Further TEM investigations (Supplementary Fig. 6) suggested that deterioration may gradually occur in the bottom BP layers while the upper BP layers continue to grow, which should be attributed to random deformation and the shifting of BP layers at high temperature[27,28]. Because a relatively high temperature of ~300 °C is required for the lateral growth of BP films, we adopted a rapid-cooling strategy after deposition, and the obtained large-area few-layer BP films were just

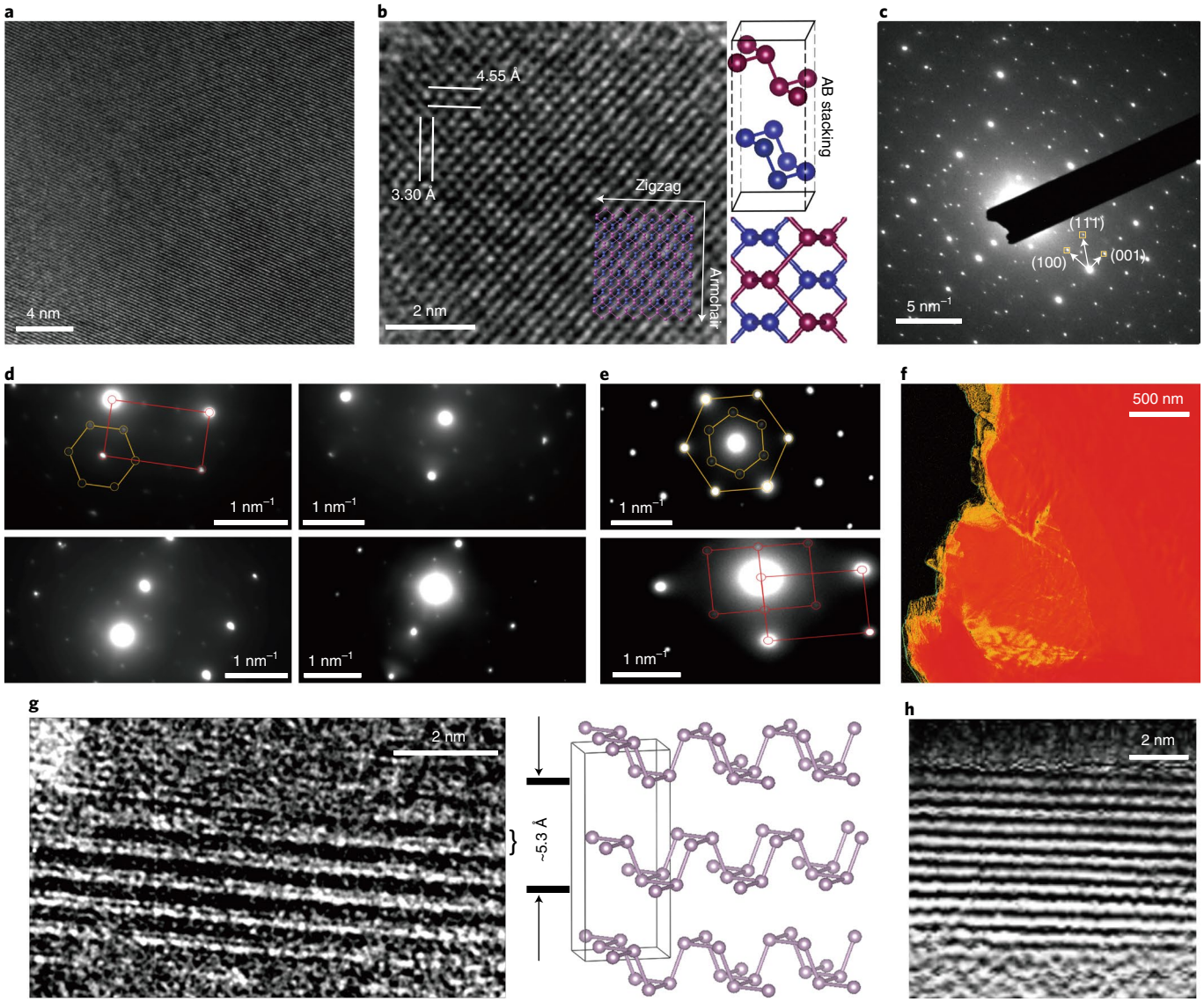

Fig. 3 | Atomistic features of few-layer BP films. a, Plan-view HRTEM image of an eight-layer BP film. A defect-free atomic structure can be recognized. **b**, Detailed HRTEM image of the BP lattice. The extracted lattice parameters match well with those of bulk single-crystal BP. Orthorhombic symmetry with AB stacking can also be recognized, as illustrated by the ball-and-stick schematics. The red and blue balls represent upper and lower BP layers within a bilayer BP structure, respectively. **c**, The corresponding SAED pattern. Crystalline features are demonstrated by the zone axis along the [010] direction. **d**,**e**, SAED patterns of four randomly selected sections of an approximate ten-layer BP (**d**), measured by DF-TEM, showing the organized stacking of the BP (red rectangle) and mica (orange hexagon) lattices by comparison with the fingerprints (**e**) of bare mica (top) and BP (bottom). **f**, The corresponding differential diffraction-filtered DF-TEM image. According to the different-colour-marked SAED patterns in **d**, the mica-orientated region is filtered with orange and the BP (010)-orientated region is in red, showing the high homogeneity of the crystal orientation distribution. **g**,**h**, Cross-sectional HRTEM images of BP films with various layer numbers. The corresponding atomic structure of the BP layers is also presented in **g**, showing a unique puckered structure with a double atomic layer within one BP layer.

adequate to satisfy the further evolution of large-scale applications at atomistic thickness.

We found that the key to the synthesis of the crystalline BP layers was to use the extreme high-temperature and high-pressure conditions created by the laser-activated plasma cloud within the confined region near the target surface to achieve energetic BP cluster formation and transportation during the non-equilibrium process of PLD (Supplementary Fig. 7). To gain theoretical insights into the formation of BP clusters, we conducted MD simulations of the laser-activated behaviour of surface BP layers on the bulk target. We first performed a series of MD simulations on the picosecond scale of the continuous ablation of BP layers under various laser fluences (Supplementary Fig. 8 and Supplementary Video 1). The results of the simulations show that the temperature and pressure within the laser-generated plasma cloud can reach over 10^3 K and 10^9 Pa, respectively, which are highly desirable for BP cluster formation[6,9]. We obtained radial distribution functions (RDFs; Supplementary Fig. 9a,b) from the MD simulations with various laser fluences; these revealed four peaks corresponding to characteristic interatomic interactions in the BP structure. The RDF curves indicate that the BP clusters are likely to form within the high-pressure region created by the controlled low-fluence pulsed laser (Supplementary Notes)[29,30], which subsequently facilitate the growth of the BP film on the substrate. In a further step toward the simulation of laser ablation on the macroscale during one complete laser pulse, the behaviour of BP clusters, including their formation and

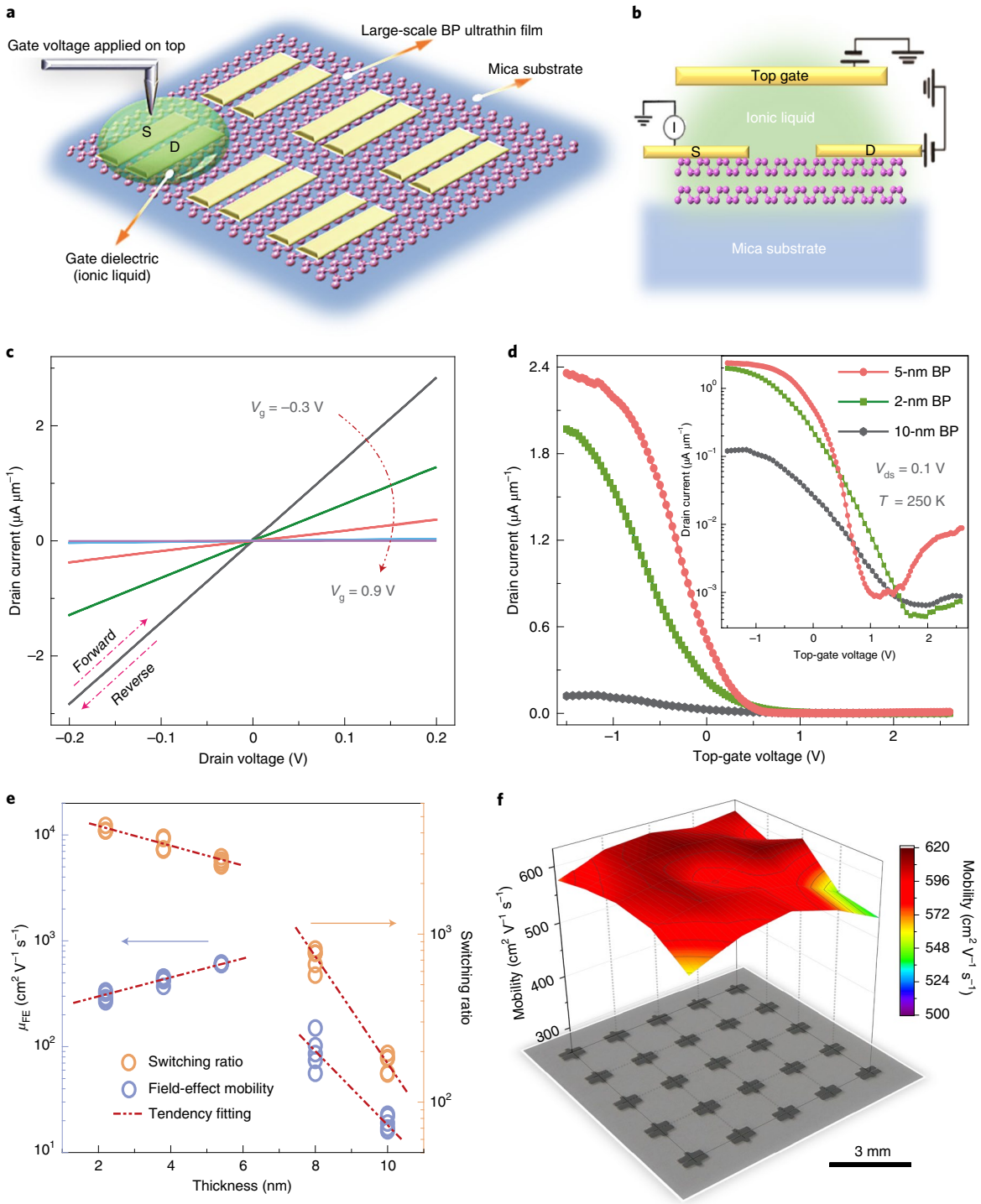

Fig. 4 | Electrical performance of centimetre-scale few-layer BP. a, Schematic of arrayed top-gated FETs based on centimetre-scale few-layer BP grown on mica substrate. S refers to source, while D refers to drain. **b**, Cross-section view of a single FET. **c**, Drain current–drain voltage (I_d–V_{ds}) curves for a FET based on a 5-nm BP ultrathin film under different gate voltages (V_g) at 250 K. **d**, Transfer characteristics of FETs based on 2-, 5- and 10-nm BP ultrathin films in linear scale at 250 K. The inset shows the same results in a logarithmic scale. **e**, Field-effect mobility (μ_{FE}) and switching ratio resulting from the FETs as a function of BP film thickness based on the results presented in **d** and further repetitive experiments. **f**, Three-dimensional colour map of carrier mobility at 250 K, extracted from 25 FETs fabricated with the same 5-nm BP sample, showing a highly uniform device performance. An optical image of the arrayed devices on top of the BP sample with a 1×1 cm^2 area is included in the figure.

transportation in the timescale of a single laser pulse, was investigated (Supplementary Fig. 9c,d and Supplementary Video 2). The results show that multilayer BP can be ablated from the target in several batches, each containing large BP clusters, under the optimal laser fluence, which is consistent with the results of our picosecond-scale simulation. Accordingly, such a laser-activated physical vapour deposition (PVD) method, differing from conventional CVD and other PVD techniques, is expected to be a feasible and powerful tool for the growth of large-scale few-layer BP films, based on the results of our combined experimental and theoretical studies.

Furthermore, FET arrays were prepared to verify the electrical performance of the as-grown BP. Benefiting from the considerable crystalline size of the as-grown BP, we fabricated FETs using hard-mask-based electron-beam deposition technology, which allows easy construction of electric devices while avoiding possible contamination or oxidation. As shown in Fig. 4a,b, 10-nm-Pd/40-nm-Au multilayers were used as electrodes. Notably, palladium was employed due to its good electrical conductivity and adhesion, as well as the suitable work function ($W_F \approx 5.2$ eV) accompanying the Fermi energy of BP ($E_F \approx 4.9$ eV) for the construction of p-type FETs. Figure 4c shows the gate-voltage-modulated current–voltage (I–V) output characteristics of a FET, from which a linear correlation can be concluded for the ohmic contact between the electrodes and BP layers. The FET performance was further studied by using an ionic liquid as a gate dielectric, which revealed typical p-type transferring behaviour with outstanding electrical performances in terms of field-effect mobility (μ_{FE}) of hole and current switching ratio (Fig. 4d,e and Supplementary Figs. 10–12). It is worth noting that BP samples with a thickness both above and below ~5 nm exhibit electrical performance (Fig. 4e). For samples thinner than 5 nm, Fig. 4e shows a linear proportional relationship between carrier mobility and film thickness. The promotion of carrier mobility can be attributed to the narrowed bandgap of the ultrathin BP layers, in accord with previous studies on other semiconductors[31]. Furthermore, the scattering and screening effects of impurities in the layered materials may also contribute to the thickness-dependent phenomenon[2]. In contrast, when the sample thickness exceeds 5 nm, a cliff-like drop in the carrier mobility emerges. Given that the inhibition of interlayer coupling is unlikely to produce such a great effect in ultrathin films, the decrease in carrier mobility is attributed to the deterioration of crystalline quality in the thicker BP samples, evidenced by the defects, such as dislocation and grain boundaries, observed under TEM. The current switching ratio shows a similar trend, with an inflection point at 5 nm. The downward trend observed for films thinner than 5 nm is mainly due to the 2D nature of the ultrathin films, that is, the modulation ability of the gate voltage tends to be suppressed for thicker layers[1]. When the film thickness exceeds 5 nm, the deterioration in the crystalline quality starts to affect the ON current, causing the slope of the curve to decline more steeply. Notably, among all the BP samples, the optimal field-effect electrical transport properties were obtained at a thickness of ~5 nm, and the carrier mobility reached up to 213 and 617 $cm^2 V^{-1} s^{-1}$ at 295 and 250 K, respectively. Such electrical performances are comparable to those of exfoliated or CVD-grown BP-based FETs of similar thickness (Supplementary Fig. 12d and Supplementary Table 1). More importantly, unlike the previously reported BP flakes with limited size, our BP films exhibit highly uniform electrical performance on the centimetre scale, according to the carrier-mobility mapping results at 25 different locations on the wafer (Fig. 4f). This attribute is of high significance in breaking through the obstacles in the scalable applications of BP, and further lay the foundation for BP applications in electronics and optoelectronics.

In summary, we have presented a controllable and rapid PLD process to directly synthesize few-layered BP on a centimetre scale with high crystallinity and homogeneity. Combined with MD simulations, an understanding of the growth mechanism of BP layer formation has been gained. We have investigated the crystal phase, crystalline quality, layered structure and energy bandgap of the as-prepared large-area BP films. Following the success of growing large-area BP films, we further fabricated few-layer BP FETs. Our large-scale BP device array exhibits appealing electrical characteristics in terms of carrier mobility and current switching ratio. These attributes are comparable to and even exceed those of exfoliated or chemically grown BP flakes with similar thickness but a much smaller scale (Supplementary Table 1). Hence, in this work we have successfully demonstrated the large-area growth of few-layer BP with a lateral size greatly increased from previously reported dozens of micrometres to the centimetre scale. It is worth noting that PLD enjoys attractive features beneficial to device fabrication, including well-controllable thickness, stoichiometric growth, high rate of growth and high compatibility with the production of multilayered heterostructures, simply by rotating multiple targets without breaking the vacuum. In contrast to much smaller-sized BP flakes fabricated by other approaches, our work opens up the possibility of further developing BP-based wafer-scale electronic and optoelectronic devices, especially scalable integrated device arrays and information systems.

Online content

Any methods, additional references, Nature Research reporting summaries, source data, extended data, supplementary information, acknowledgements, peer review information; details of author contributions and competing interests; and statements of data and code availability are available at https://doi.org/10.1038/s41563-021-01001-7.

Received: 2 September 2020; Accepted: 1 April 2021;
Published online: 10 May 2021

References

1. Li, L. et al. Black phosphorus field-effect transistors. *Nat. Nanotechnol.* **9**, 372–377 (2014).
2. Qiao, J., Kong, X., Hu, Z. X., Yang, F. & Ji, W. High-mobility transport anisotropy and linear dichroism in few-layer black phosphorus. *Nat. Commun.* **5**, 4475 (2014).
3. Xia, F., Wang, H. & Jia, Y. Rediscovering black phosphorus as an anisotropic layered material for optoelectronics and electronics. *Nat. Commun.* **5**, 4458 (2014).
4. Liu, H. et al. Phosphorene: an unexplored 2D semiconductor with a high hole mobility. *ACS Nano* **8**, 4033–4041 (2014).
5. Lowndes, D. H., Geohegan, D. B., Puretzky, A. A., Norton, D. P. & Rouleau, C. M. Synthesis of novel thin-film materials by pulsed laser deposition. *Science* **273**, 898–903 (1996).
6. Shriber, P., Samanta, A., Nessim, G. D. & Grinberg, I. First-principles investigation of black phosphorus synthesis. *J. Phys. Chem. Lett.* **9**, 1759–1764 (2018).
7. Gaufrès, É. et al. Momentum-resolved dielectric response of free-standing mono-, bi-, and trilayer black phosphorus. *Nano Lett.* **19**, 8303–8310 (2019).
8. Li, L. et al. Direct observation of the layer-dependent electronic structure in phosphorene. *Nat. Nanotechnol.* **12**, 21–25 (2017).
9. Liu, H., Du, Y., Deng, Y. & Ye, P. D. Semiconducting black phosphorus: synthesis, transport properties and electronic applications. *Chem. Soc. Rev.* **44**, 2732–2743 (2015).
10. Wang, X. et al. Highly anisotropic and robust excitons in monolayer black phosphorus. *Nat. Nanotechnol.* **10**, 517–521 (2015).
11. Youngblood, N., Chen, C., Koester, S. J. & Li, M. Waveguide-integrated black phosphorus photodetector with high responsivity and low dark current. *Nat. Photonics* **9**, 247–252 (2015).
12. Wu, Z. & Hao, J. Electrical transport properties in group-V elemental ultrathin 2D layers. *NPJ 2D Mater. Appl.* **4**, 1–13 (2020).
13. Chen, L. et al. Scalable clean exfoliation of high-quality few-layer black phosphorus for a flexible lithium ion battery. *Adv. Mater.* **28**, 510–517 (2016).
14. Hanlon, D. et al. Liquid exfoliation of solvent-stabilized few-layer black phosphorus for applications beyond electronics. *Nat. Commun.* **6**, 8563 (2015).
15. Li, C. et al. Synthesis of crystalline black phosphorus thin film on sapphire. *Adv. Mater.* **30**, 1703748 (2018).
16. Smith, J. B., Hagaman, D. & Ji, H. F. Growth of 2D black phosphorus film from chemical vapor deposition. *Nanotechnology* **27**, 215602 (2016).
17. Xu, Y. et al. Epitaxial nucleation and lateral growth of high-crystalline black phosphorus films on silicon. *Nat. Commun.* **11**, 1330 (2020).
18. Tian, B. et al. Facile bottom-up synthesis of partially oxidized black phosphorus nanosheets as metal-free photocatalyst for hydrogen evolution. *Proc. Natl Acad. Sci. USA* **115**, 4345–4350 (2018).
19. Castellanos-Gomez, A. et al. Isolation and characterization of few-layer black phosphorus. *2D Mater.* **1**, 025001 (2014).
20. Kim, Y. et al. Remote epitaxy through graphene enables two-dimensional material-based layer transfer. *Nature* **544**, 340–343 (2017).

21. Xu, X. et al. Atomic-precision repair of a few-layer 2H-$MoTe_2$ thin film by phase transition and recrystallization induced by a heterophase interface. *Adv. Mater.* **32**, 2000236 (2020).
22. Zhang, S. et al. Extraordinary photoluminescence and strong temperature/angle-dependent Raman responses in few-layer phosphorene. *ACS Nano* **8**, 9590–9596 (2014).
23. Guo, Z. et al. From black phosphorus to phosphorene: basic solvent exfoliation, evolution of Raman scattering, and applications to ultrafast photonics. *Adv. Funct. Mater.* **25**, 6996–7002 (2015).
24. Favron, A. et al. Photooxidation and quantum confinement effects in exfoliated black phosphorus. *Nat. Mater.* **14**, 826–832 (2015).
25. Lei, S., Wang, H., Huang, L., Sun, Y. Y. & Zhang, S. Stacking fault enriching the electronic and transport properties of few-layer phosphorenes and black phosphorus. *Nano Lett.* **16**, 1317–1322 (2016).
26. Morita, A. Semiconducting black phosphorus. *Appl. Phys. A* **39**, 227–242 (1986).
27. Lin, S. et al. In situ observation of the thermal stability of black phosphorus. *2D Mater.* **4**, 025001 (2017).
28. Liu, X., Wood, J. D., Chen, K. S., Cho, E. & Hersam, M. C. In situ thermal decomposition of exfoliated two-dimensional black phosphorus. *J. Phys. Chem. Lett.* **6**, 773–778 (2015).
29. Sha, W, Wu, X & Keong, K. G. in *Electroless Copper and Nickel-Phosphorus Plating* Ch. 6 (Woodhead Publishing, 2011).
30. Brown, A. & Rundqvist, S. Refinement of the crystal structure of black phosphorus. *Acta Crystallogr.* **19**, 684–685 (1965).
31. Schwierz, F. Graphene transistors. *Nat. Nanotechnol.* **5**, 487–496 (2010).

Methods

Growth of centimetre-scale few-layer BP films. First, surface stripping of the mica substrate was carried out before it was mounted in the growth chamber, which guaranteed a fresh and spotless substrate surface for subsequent BP deposition. Afterwards, the source (BP single crystal, SMART-ELEMENTS) and substrate were placed face to face in the chamber, with a separation distance of ~36 mm. The chamber was then pumped to an ultrahigh vacuum of ~1.6×10^{-9} torr and the mica substrate was heated to 300 °C. A plasma plume containing large BP clusters was generated from the target by using a KrF excimer pulsed laser ($\lambda=248$ nm) with a repetition rate of 5 Hz and a laser fluence of 1.2 J cm^{-2}. The physical vapour containing ablated clusters was then transmitted towards the surface of the mica substrate and a few-layer BP film was formed under a controlled substrate temperature. The mica substrate was rotated throughout the growing process to achieve uniform deposition, and the BP source was fixed to maintain the uniformity and stability of the plasma plume. After deposition, the temperature of the as-synthesized BP film was immediately and rapidly cooled to room temperature (RT) by venting dry N_2 gas into the growth chamber and moving the sample holder away from the heater. To prove the effectiveness of the rapid-cooling approach, we experimentally investigated the cooling rates achieved by natural and rapid cooling (Supplementary Fig. 1); the results showed that the cooling rate was obviously promoted by the rapid-cooling strategy. To avoid degradation of the as-prepared few-layer BP films, the samples were transferred for subsequent study in sealed containers filled with protection gas.

Bulk single-crystal BP was used as the source material for the deposition to inhibit the ejection of heterogeneous large particles or droplets, which enabled the formation of BP films with well-defined morphology. This laser-ablated ejection model has been demonstrated for a wide variety of source materials in previous studies on laser ablation processing, especially for those substances that can barely form dense and uniform targets[32,33]. Regarding the substrate for deposition, freshly exfoliated mica was used to facilitate epitaxial growth of the BP film. Recently, mica substrate has come to be considered a promising candidate for vdW epitaxial growth of 2D materials. Owing to the 2D nature of mica, its freshly exfoliated surface possesses satisfactory atomic planeness and surface inertness, allowing a low migration barrier energy for 2D material growth[34–38].

Growth of monolayer triangular MoS_2. MoS_2 nanosheets of fine triangular shape were synthesized by the CVD method. A powder mixture of 10 mg MoO_3 and 5 mg NaCl in a quartz boat was placed in the centre of a quartz tube. Then, 20 mg sulfur powder was placed upstream of the furnace at 180 °C. Prior to crystal growth, the quartz tube was evacuated to below 6 Pa and flushed with argon carrier gas. The furnace was then heated to the growing temperature (750 °C) at a ramp rate of 15 °C min^{-1} and held at that temperature for 10 min before allowing to cool naturally to RT. Argon carrier gas at a flow rate of 60 cm^3 min^{-1} was used to facilitate crystal growth.

Model settings for the MD simulations. MD simulations were performed using a large-scale atomic/molecular massively parallel simulator to simulate the laser influence during the PLD process. The BP layer was modelled with active layers on the top and two fixed layers at the bottom. Laser heating was simulated by imposing a constant heat fluence to the active BP layers while keeping the position of the fixed layers stationary. Periodic boundary conditions were imposed along the in-plane x and y directions to eliminate the edge effect, and a vacuum layer with sufficient thickness was applied along the out-of-plane z direction. The Stillinger–Weber potential was applied in the simulations to define the intralayer P–P bonds. The parametrization of the Stillinger–Weber potential for phosphorene was based on the ab initio valence force-field (VFF) model of Jiang[39]. For the interlayer interactions between adjacent BP layers, the 12-6 Lennard-Jones (LJ) potential ($V(r)$) was employed:

$$V(r) = 4\varepsilon\left[\left(\frac{\sigma}{r}\right)^{12} - \left(\frac{\sigma}{r}\right)^{6}\right] \quad (1)$$

where r is the separation between two particles. The energy constant ε and distance constant σ were obtained from the universal force field[40], where $\varepsilon=0.0132$ eV and $\sigma=3.695$ Å. The cut-off distance for the LJ potential was set as 15 Å.

During the simulations, a time step of 0.5 fs was used to integrate the equations of motion. The initial configuration was first subjected to energy minimization at 0 K using the conjugate gradient method. System equilibration was then carried out at 300 K with Nosé–Hoover thermostats to release internal stresses in the BP structure. Upon equilibration, the system was switched to a microcanonical ensemble (that is, an *NVE* ensemble, where *N*, *V* and *E* refer to the constant number of particles, volume and total energy, respectively) for laser heating. For the simulation of the continuous ablation of BP segments from the target, BP with lateral dimensions of 100×100 Å^2 with two active layers and a 200-Å vacuum layer was modelled. Laser heating was carried out for 10 ps for the ablation of segments before the cluster-formation simulations. With the effect of laser heating, the ablated phosphorus segments were extracted for BP cluster formation. To simulate dynamic bond creation, a harmonic bond potential was defined according to the VFF model[41]. The bond-stretching (V_r) and angle-bending (V_θ) potentials can be described by:

$$V_r = \frac{1}{2}K_r(r-r_0)^2 \quad (2)$$

$$V_\theta = \frac{1}{2}K_\theta r_1 r_2(\theta-\theta_0)^2 \quad (3)$$

where K_r and K_θ are the valence force constants, r_0, r_1 and r_2 are the equilibrium bond distances, and θ_0 is the equilibrium angle. Accordingly, we used $r_0=2.224$ Å and $K_r=7.578$ eV Å^{-2} for the bonds, $\theta_0=96.359°$, $r_1=r_2=2.224$ Å and $K_\theta=0.818$ eV Å^{-2} for angle I (zigzag), and $\theta_0=102.090°$, $r_1=r_2=2.224$ Å and $K_\theta=0.710$ eV Å^{-2} for angle II (armchair), respectively, in our simulations[41]. Here, we assumed that all the bonds in the BP structure have identical length and stretching parameters. The LJ potential was adopted to define the vdW force between all the phosphorus atoms. To guarantee that the ablated segments reached steady state, the system was equilibrated before data collection. The RDFs were obtained by averaging multiple measurements in the steady state.

For the MD simulation of laser ablation during one complete laser pulse, the BP target surface was imitated using 48 active layers, which guaranteed no residual laser energy within one laser pulse. A 14,000-Å vacuum layer was applied along the out-of-plane direction to enable complete transportation of BP clusters. The laser heating was carried out for 2 ns. The atomistic data from the MD simulations were visualized and analysed using the OVITO package[42].

Material characterization methods. Raman investigations were carried out with high-resolution confocal μ-Raman microscopes (Horiba HR 800 and Witec alpha300 R) equipped with 488- and 532-nm laser sources. To preserve the crystalline structure of the BP samples, the samples were placed in ~10^{-3} torr vacuum capsules with a transparent test window, and the laser power through a ×100 (numerical aperture, NA = 0.9) objective was controlled at a low level of ~1 μW. Accordingly, the optical resolutions of the Raman microscopes were ~360 nm (for $\lambda=532$ nm) and ~330 nm (for $\lambda=488$ nm). The thicknesses and surface morphologies of the few-layer BP films were studied with a commercial atomic force microscope (Asylum Research MFP-3D). PL measurements were conducted with an FLS920P Edinburgh Analytical Instrument equipped with an 808-nm diode laser (MDL-808) as excitation source. The crystal structures of the as-prepared samples were characterized by X-ray diffraction (Rigaku SmartLab, 9 kW) using Cu Kα radiation ($\lambda=1.5406$ Å). XPS was performed with a Thermo Scientific Nexsa X-ray photoelectron spectrometer equipped with a monochromatic and focused 12-kV Al Kα X-ray source. Scanning electron microscopy (SEM) and EBS images were obtained with a Tescan VEGA3 scanning electron microscope with the electron voltage controlled at 5 kV. EBSD measurements were carried out with a field-emission-gun scanning electron microscope (LEO 1530) equipped with an EBSD detector (Oxford Instruments NordlysNano EBSD detector and AZtecHKL) with fine adjustment of the tilt angle between 60.7° and 70.3°, and the electron voltage controlled at 20 kV. Before the EBSD measurements, the bottom mica layer was reduced by tape exfoliation. Then, a 10-nm conductive carbon layer was constructed in the form of a gridded frame on top of the sample by mask-assisted deposition, and conductive silver paste was used to cover the boundary between the sample and holder. This construction process aimed to reduce surface electron accumulation during measurement, while less intrusive signals could be obtained from the regions exposed on the grid. The microstructures and chemical compositions of the as-prepared BP films were further investigated by field-emission scanning transmission electron microscopy (JEOL Model JEM-2100F) in conjunction with EDX using an accelerating voltage of 100 kV and an exposure time of 0.3 s. In the differential diffraction-filtered colour imaging used for DF-TEM mapping, regions with mica-orientated signals are filled in orange and the (010)-orientated BP signals are filled in red, in accord with the previously defined electron diffraction patterns of each lattice. The areas of BP and mica with homogeneous crystal orientation were derived by stacking the constructed bitmaps, while the boundaries and vacuum (or carbon membrane) are represented by the dark area. Specimens for HRTEM measurements were prepared by the polystyrene-mediated transfer approach with ethanol-assisted lift-off. Specimens for cross-section TEM measurements were obtained using focused ion-beam (FIB, JEOL JIB-4500) milling and lift-off. All the obtained samples were transferred to copper grids for TEM characterization.

Device fabrication methods. Following the deposition and rapid-cooling process, the mica-based few-layer BP films were covered with the hard-mask templates (made of highly purified molybdenum) of the designed patterns and transferred to the electron-beam deposition chamber (Denton Vacuum E-beam Explorer System) under dry N_2 protection. Then, a 10-nm-Pd/40-nm-Au multilayer metal contact was deposited on the top of the BP films to form the source, drain and gate electrodes. The growth rates of the Pd and Au layers were carefully controlled at 0.2 and 0.7 Å s^{-1}, respectively, to avoid potential damage to the surface of the BP layers. Typically, the channel length of the obtained FETs was 40 μm and the channel width was 400 μm. Prior to measurement, one droplet of ionic liquid (diethylmethyl(2-methoxyethyl)ammonium bis(trifluoromethylsulfonyl) imide, DEME-TFSI, Sigma Aldrich 727679) was carefully placed on top of the

construction using a micromanipulator under an optical microscope, covering the source, drain and gate electrodes. After dehydration, an ionic-liquid gate–dielectric layer was formed by self-assembly, yielding a top-gated FET.

Device characterization methods. After fabrication, the devices were cooled to 250 K and maintained at this temperature for a few minutes in a vacuum of 6×10^{-7} torr to freeze the water in the ionic liquid before characterization. Although the voltage applied in our experiments was relatively low, the tests at low temperature further excluded the possibility of water electrolysis during measurement, which may cause degradation of the intrinsic electrical properties of BP. The device was characterized at 250 K using a Keithley 4200 Semiconductor Parameter Analyzer equipped with a probe station (Lake Shore Model CRX-6.5K) connected to a vacuum chamber, a liquid helium cryogenic test platform (Lake Shore Model 336 Cryogenic Temperature Controller), a micromanipulator with 5-μm tips and an optical microscope. It is worth noting that, to demonstrate the sheer electrostatic field-effect phenomena and avoid any interfacial electrochemical reaction or intercalation[43], the electrical characteristics reported in the main text were measured within the recognized electrostatic working window of DEME-TFSI at a low temperature of ~250 K and a small voltage of less than 2 V. Additionally, because semiconductor devices are usually operated at RT in real applications, we also studied the performance of our BP-based FETs at RT (Supplementary Fig. 12a,b). Because the theoretical electrolytic voltage of water is around 1.5 V (greater than 2.1 V if heat balance is considered), the performance of our devices was verified within a voltage range below this critical value, that is, at voltages that ensured that water was not ionized. Characterization was conducted in a dark environment to prevent ambient light influencing the measured electrical properties of BP.

Determination of the capacitance density of the ionic liquid. To guarantee the accuracy and reliability of the electrical performance measurements, relatively stable and conventional MoS_2 nanosheets were employed for comparison. As analogues of the BP-based top-gated FETs, we constructed MoS_2-based devices using CVD-grown triangular MoS_2 samples on 300-nm SiO_2/Si substrates. Supplementary Fig. 10 illustrates the process used to determine the capacitance density (capacitance per unit area) of the ionic-liquid droplet[44]. As shown in Supplementary Fig. 10c, the underlying silicon layer acts as the back-gate electrode of the FETs with the 300-nm SiO_2 substrate as the dielectric, and the Pd/Au electrodes deposited on top of the MoS_2 act as the source, drain and top gate, with a droplet of the ionic liquid on top of these three electrodes acting as the dielectric. When a drain voltage (V_{ds}) and top-gate voltage (V_{tg}) were applied to a representative FET, a transfer characteristic curve was obtained (Supplementary Fig. 10d). Supplementary Fig. 10e shows the evolution of the FET output curve when various back-gate voltages (V_{bg}) were applied. The drain-current (I_d)–V_{tg} curves show that the most affected parameter is the threshold voltage (V_{th}): as V_{bg} gradually increases from 0 to 30 V, the corresponding V_{th} systematically shifts to a more negative V_{tg}, whereas the slopes of the I_d–V_{tg} curve within the linear work region remain nearly constant. The capacitance density of the ionic liquid ($C_{tg\text{-}IL}$) can be estimated on the basis on the change in V_{th} (ΔV_{th}) in response to the variation in V_{bg} (ΔV_{bg}):

$$C_{tg-IL}/C_{bg} = \Delta V_{bg}/\Delta V_{th} \quad (4)$$

where $C_{bg} = 1.2\times10^{-8}$ F cm^{-2} is the capacitance density of the SiO_2 (back-gate dielectric) and $\Delta V_{bg}/\Delta V_{th} = 120$, extracted by linear fitting (Supplementary Fig. 10f). Accordingly, the capacitance density of the ionic-liquid droplet was estimated to be $C_{tg\text{-}IL} \approx 1.44\times10^{-6}$ F cm^{-2}.

Calculation of field-effect mobility. The field-effect carrier mobility (μ_{FE}) of the large-scale few-layer BP films can be extracted from the transport characteristic curves of the top-gated FETs:

$$\mu_{FE} = \frac{L}{WC_{tg-IL}V_{ds}}\frac{dI}{dV} \quad (5)$$

where L is the channel length (40 μm), W is the channel width (400 μm), $C_{tg\text{-}IL} \approx 1.44\times10^{-6}$ F cm^{-2} and dI/dV is the field-gating efficiency obtained by matching the slope of the curve within the linear work region. Due to the fixed dosage of ionic liquid employed in the device fabrication, the contributing capacitance density used for the mobility calculation can be considered as a constant[44].

Construction of a back-gated BP FET through encapsulated transfer. Supplementary Fig. 11 shows the construction of a back-gated BP FET conducted in a dry glovebox filled with high-purity nitrogen. After the growth of a large-scale BP ultrathin film on mica substrate through PLD, a device array with Pd/Au electrodes was fabricated by electron-beam deposition. Then, a pre-prepared hexagonal boron nitride film was placed on top of the constructed BP device through a dry transfer process to form an encapsulation layer. The top surface of the sample was then coated with a poly(vinyl alcohol)/poly(methyl methacrylate) (PVA/PMMA) supporting membrane. Notably, the size of the PVA membrane should be larger than that of the sample to keep the sample suspended in ethanol during the following process. Afterwards, we gently immersed the sample into ethanol and kept the mica in suspension. Because the mica substrate and BP film are bound together by vdW forces, the ethanol was able to slowly penetrate into their interface and separate them. Under the force of gravity, mica tends to sink in the ethanol, whereas the PVA/PMMA-supported sample remains in suspension, further increasing the stripping rate. When the mica had completely sunk, we removed it and placed a new SiO_2/Si substrate under the suspended sample. Finally, we used a syringe to slowly draw the ethanol away, allowing the sample to be released flat onto the target substrate to construct a back-gated BP FET array after drying and fixation.

Data availability

The authors declare that the data supporting the findings of this study are available within the paper and its Supplementary Information files.

References

32. von Wenckstern, H. et al. Continuous composition spread using pulsed-laser deposition with a single segmented target. *Cryst. Eng. Commun.* **15**, 10020 (2013).
33. Li, Y., Yao, X. & Tanabe, K. Improved surface morphology of $NdBa_2Cu_3O_{7-\delta}$ films grown by pulsed laser deposition using a large single crystal target. *Physica C* **304**, 239–244 (1998).
34. Huang, W. et al. Controlled synthesis of ultrathin 2D β-In_2S_3 with broadband photoresponse by chemical vapor deposition. *Adv. Funct. Mater.* **27**, 1702448 (2017).
35. Wen, Y. et al. Epitaxial 2D PbS nanoplates arrays with highly efficient infrared response. *Adv. Mater.* **28**, 8051–8057 (2016).
36. Zhou, Y. et al. Epitaxy and photoresponse of two-dimensional GaSe crystals on flexible transparent mica sheets. *ACS Nano* **8**, 1485–1490 (2014).
37. Koma, A. Van der Waals epitaxy for highly lattice-mismatched systems. *J. Cryst. Growth* **201**, 236–241 (1999).
38. Lui, C. H., Liu, L., Mak, K. F., Flynn, G. W. & Heinz, T. F. Ultraflat graphene. *Nature* **462**, 339–341 (2009).
39. Jiang, J. W. Parametrization of Stillinger–Weber potential based on valence force field model: application to single-layer MoS_2 and black phosphorus. *Nanotechnology* **26**, 315706 (2015).
40. Rappé, A. K., Casewit, C. J., Colwell, K. S., Goddard, W. A. & Skiff, W. M. UFF, a full periodic table force field for molecular mechanics and molecular dynamics simulations. *J. Am. Chem. Soc.* **114**, 10024–10035 (1992).
41. Kaneta, C., Katayama-Yoshida, H. & Morita, A. Lattice dynamics of black phosphorus. *Solid State Commun.* **44**, 613–617 (1982).
42. Stukowski, A. Visualization and analysis of atomistic simulation data with OVITO – the Open Visualization Tool. *Modell. Simul. Mater. Sci. Eng.* **18**, 015012 (2010).
43. Shiogai, J., Ito, Y., Mitsuhashi, T., Nojima, T. & Tsukazaki, A. Electric-field-induced superconductivity in electrochemically etched ultrathin FeSe films on $SrTiO_3$ and MgO. *Nat. Phys.* **12**, 42–46 (2016).
44. Perera, M. M. et al. Improved carrier mobility in few-layer MoS_2 field-effect transistors with ionic-liquid gating. *ACS Nano* **7**, 4449–4458 (2013).

Acknowledgements

This work was supported by grants from the National Natural Science Foundation of China (nos. 51972279 and 11534010) and the Research Grants Council of Hong Kong (GRF nos. PolyU 153025/19P and PolyU 153039/17P) and a PolyU Grant (1-ZVGH).

Author contributions

J.H., Z.W. and X.H.C. conceived the original idea and designed the experiments. J.H., S.P.L. and X.H.C. supervised the project. Z.W. and B.Z. developed the synthesis techniques and fabricated the samples. Y.L. performed the MD simulations. Z.W. and Y.Z. conducted the TEM and EDX experiments. Z.W. and R.D. performed other physical characterizations, including the AFM, EBS, XPS, XRD, EBSD, Raman, PL and SEM studies, and analysed the results. Z.W. and Z.Y. fabricated the FET devices and investigated their electrical properties. Z.W., Y.L., X.H.C. and J.H. co-wrote the paper and all the authors commented on it.

Competing interests

The authors declare no competing interests.

Additional information

Supplementary information The online version contains supplementary material available at https://doi.org/10.1038/s41563-021-01001-7.

Correspondence and requests for materials should be addressed to X.H.C. or J.H.

Peer review information *Nature Materials* thanks Richard Martel, Amin Salehi-Khojin and the other, anonymous, reviewer(s) for their contribution to the peer review of this work.

Reprints and permissions information is available at www.nature.com/reprints.